International Journal of Nanomedicine

Dovepress
Taylor & Francis Group

Open Access Full Text Article

ORIGINAL RESEARCH

Two-Dimensional MXenes Surface Engineering Nanoplatform for PTT-Chemotherapy Synergistic Tumor Therapy

Yang Dong[1,2,*], Liang Guo[3,*], Lu Song[1], Tingting Liu[1], Gang Zheng[2], Meizhu Zheng[2], Baojiang Li[1]

[1]Department of Breast Surgery, Breast Cancer Center, The Affiliated Taian City Central Hospital of Qingdao University, Taian, Shandong, 271000, People's Republic of China; [2]Department of Breast Surgery, Shandong Cancer Hospital and Institute, Shandong First Medical University and Shandong Academy of Medical Sciences, Jinan, Shandong, 250117, People's Republic of China; [3]Department of Thoracic Surgery, Shanghai Pulmonary Hospital, Tongji University School of Medicine, Shanghai, 200433, People's Republic of China

*These authors contributed equally to this work

Correspondence: Baojiang Li, Department of Breast Surgery, Breast Cancer Center, The Affiliated Taian City Central Hospital of Qingdao University, Taian, Shandong, 271000, People's Republic of China, Email libaojiang28@sina.com; Meizhu Zheng, Department of Breast Surgery, Shandong Cancer Hospital and Institute, Shandong First Medical University and Shandong Academy of Medical Sciences, Jinan, Shandong, 250117, People's Republic of China, Email zheng_0624@163.com

Background: Triple-negative breast cancer (TNBC) has a high early recurrence rate and poor prognosis. Given its insensitivity to traditional systemic chemotherapy, there is an urgent need for new therapeutic strategies for effective treatment. This paper reports the development of a novel two-dimensional MXene composite nanoplatform for efficient synergistic chemotherapy and photothermal therapy of TNBC.

Results: To achieve surface functionalization of MXene, we developed a surface nanopore engineering strategy, enabling the uniform coating of a thin mesoporous silica layer on the two-dimensional Ti_3C_2 MXene surface. This strategy endows MXenes with well-defined mesopores for on-demand drug release/delivery and enhanced hydrophilicity/dispersibility. Systematic in vitro and in vivo evaluations demonstrate that Ti_3C_2@MSNs have high active targeting capability upon entering tumors, and through the synergistic chemotherapy of the mesoporous shell and the photothermal therapy of the Ti_3C_2 MXene core, tumors can be completely eradicated with no significant recurrence.

Conclusion: This study provides a new strategy for developing MXene-based composite nano drug delivery systems to effectively combat TNBC.

Keywords: photothermal therapy, chemotherapy, Ti_3C_2 MXene, mesoporous silica, synergistic therapy

Introduction

Triple-negative breast cancer (TNBC) is characterized by the absence of estrogen receptors (ER) and progesterone receptors (PR), as well as the lack of overexpression and/or gene amplification of ERBB2 (HER2).[1] It mostly presents in the form of high-grade invasive ductal carcinoma, with a high early recurrence rate and a poorer prognosis compared to other subtypes of breast cancer. Currently, the treatment of TNBC relies on chemotherapy, mainly based on anthracyclines, taxanes, and/or platinum-based drugs.[2–4] However, due to the high intratumoral heterogeneity of TNBC, patients often experience inherent chemotherapy resistance and severe side effects, and the clinical treatment outcomes of TNBC remain unsatisfactory. Therefore, there is an urgent need for new treatment approaches to manage TNBC.

Safe, stable, and efficient nanomedical materials have gained momentum in the treatment of various types of malignant tumors (including TNBC).[5] Targeting the microenvironment characteristics of TNBC, nano-carriers with good stability and targeting ability have been constructed.[6] They are combined with novel treatment methods such as sonodynamic therapy, photodynamic therapy, and photothermal therapy (PTT), showing great potential in the treatment

Received: 27 August 2024
Accepted: 18 December 2024
Published: 14 February 2025

Graphical Abstract

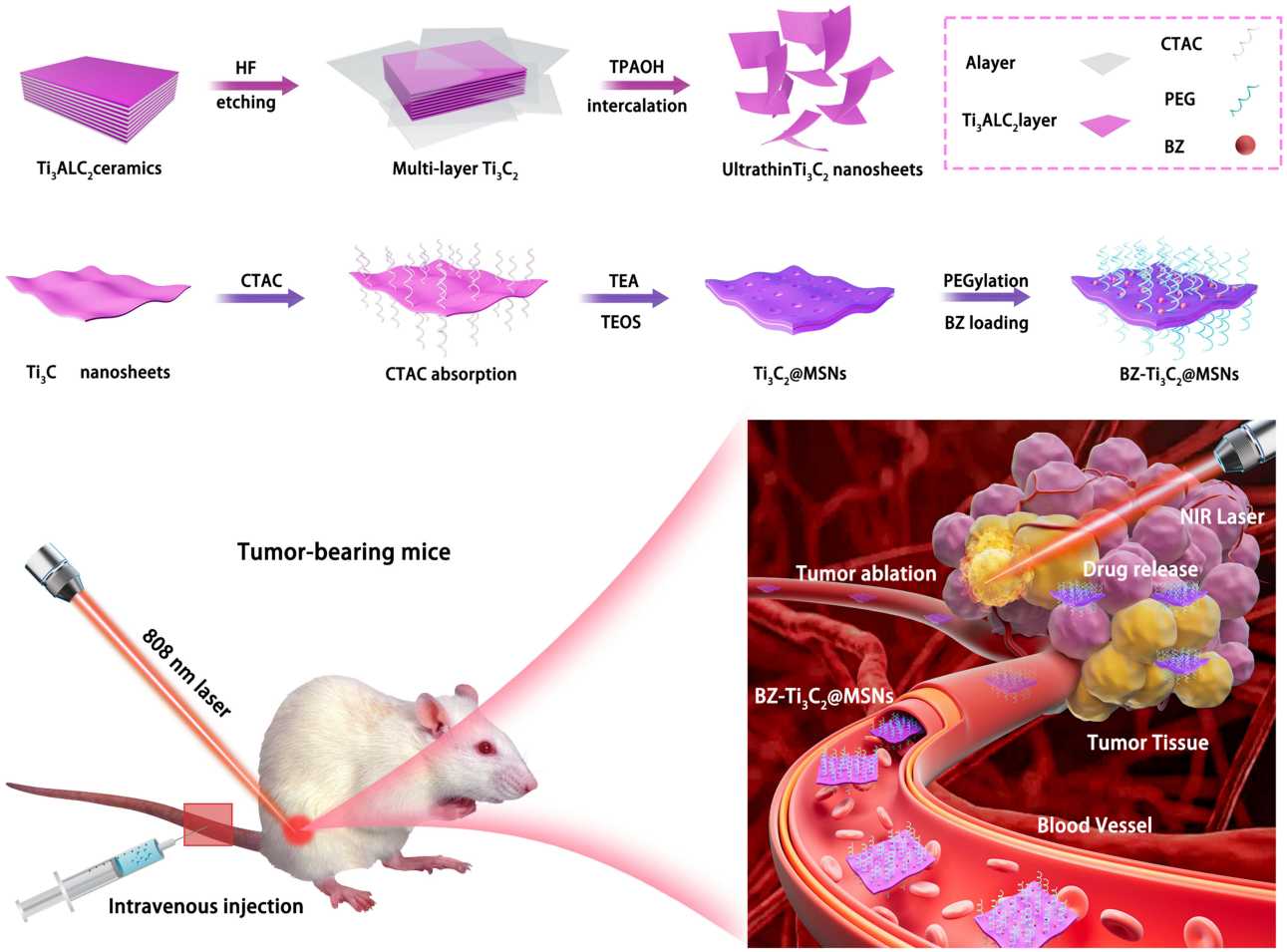

of TNBC.[7,8] PTT is widely recognized for its minimal damage to normal tissues and high ablation efficiency.[9–11] It is usually triggered by photothermal transducers (PTAs) under near-infrared (NIR) laser, generating heat in situ to thermally ablate cancer cells.[12–14] It is worth noting that the administration system of these PTAs can significantly enhance the synergistic therapeutic effect of tumor ablation and chemotherapy, enhancing tumor sensitivity.[15,16]

In the past few years, two-dimensional (2D) layered nanomaterials have attracted great attention in the scientific community. Their unique ultra-thin layered structure and excellent physicochemical properties enable them to have extensive applications in various research fields, including the treatment of diseases such as tumors, energy conversion, and photoelectrochemical catalysis.[17–19] MXene is an emerging member of the two-dimensional layered material family, composed of transition metal carbides and carbon/nitride compounds, which are bioceramic materials. Since Gogotsi Yury et al obtained MXene through HF etching and delamination methods in 2011, the potential value of MXene in various fields has been gradually explored, including energy storage, ion sieves, etc.[20] Research on 2D MXene nanosheets in the past two years has demonstrated their ultra-high biocompatibility and unique diagnostic and therapeutic properties, such as photothermal therapy (PTT), diagnostic imaging, and antibacterial characteristics.[21–23] In particular, two-dimensional Ti_3C_2 MXene nanosheets have been proven to be ideal photothermal conversion nanoreagents, and their high biocompatibility ensures further clinical translation. Compared with traditional tumor treatment methods (surgery, chemotherapy, radiotherapy), PTT, as a new non-invasive tumor treatment method, has the advantages of high efficacy

and minimal systemic side effects.[12,24] PTT usually irradiates specific tumor sites to absorb near-infrared (NIR) laser and convert it into local high temperature, thereby achieving irreversible ablation of tumor tissues. Many organic/inorganic nanomaterials with high photothermal conversion performance have developed rapidly in recent years, including carbon-based nanomaterials, transition metal sulfides, BP, organic nanoparticles (such as porphyrins, indocyanine green, and melanin), and emerging MXene nanosheets.[25–28] However, research has only shown that Ti_3C_2 MXene has a local high temperature effect that can cause tumor ablation, thereby achieving efficient treatment of cancer, achieving more precise treatment effects, and enhancing treatment safety. Due to its large surface area, MXene is expected to be an ideal nanocarrier for drug delivery and chemotherapy.[29,30] However, the lack of enclosed spaces for these drug molecules makes it difficult for drugs to be loaded. Furthermore, the surface of MXene lacks functional groups for modification, posing significant challenges for possible targeted modifications and surface engineering for specific purposes (such as targeted delivery/therapy). Bevacizumab (BZ) is a large-molecule monoclonal antibody drug belonging to the class of vascular endothelial growth factor inhibitors.[31–33] It can effectively bind to vascular endothelial growth factor in tumor cells, thereby blocking the mitotic activity of endothelial cells, inhibiting the formation of blood vessels in tumors, and ultimately inhibiting the growth of tumors by reducing the blood supply to tumor cells.[34] However, as a large-molecule drug, it is prone to proteolytic degradation after oral administration, losing its effectiveness in the intestines.

Therefore, in this study, we designed and prepared surface nano-engineered two-dimensional Ti_3C_2 MXene based on simple and easy sol-gel chemistry for intravenous delivery of the drug bevacizumab (BZ). Specifically, under alkaline synthesis conditions, with cetyltrimethylammonium chloride (CTAC) as the mesoporous directing agent and tetraethyl orthosilicate (TEOS) as the silicon precursor, a thin mesoporous silica shell was successfully coated on the surface of Ti_3C_2 MXene (Ti_3C_2@MSNs). Coating mesoporous silica vertically onto two-dimensional Ti_3C_2 nanosheets can improve the interfacial properties of Ti_3C_2 MXene. By combining these two materials as drug delivery carriers and photothermal conversion nanoreagents, advantages include well-defined mesopores for loading bevacizumab (BZ) with narrow spaces, enhanced hydrophilicity and dispersibility, and abundant surface chemical species available for further modification and engineering. Therefore, these carefully designed 2D Ti_3C_2@MSNs composite materials are expected to exert specific functions for synergistic chemotherapy and photothermal ablation therapy of TNBC.

Materials and Methods

Materials

Hexadecyltrimethylammonium chloride (CTAC) and Tetrapropylammonium hydroxide (TPAOH) were purchased from Shanghai Aladdin Biochemical Technology Co., Ltd. Hydrofluoric acid (HF) aqueous solution (60 mL, 40%) was purchased from Sinopharm Chemical Reagents Co., Ltd., Shanghai, China. Ti_3AlC_2 ceramics powders was obtained from Forsman Scientific (Beijing) Co., Ltd. Triethanolamine (TEA), and Tetraethyl orthosilicate (TEOS) were purchased from Macklin Biochemical Technology Co., Ltd., Shanghai, China. Erythrocytes were purchased from Shanghai yuanye Bio-Technology Co., Ltd Shanghai, China. Fetal bovine serum (FBS) was purchased from Biological Industries. Cell Counting Kit-8 (CCK-8), Calcein/PI Cell Viability/Cytotoxicity Assay Kit and DAPI dihydrochloride were obtained from Beyotime Biotech Inc., China.

Synthesis of Ti_3C_2 Nanosheets

After immersing 10 grams of Ti_3AlC_2 powder in a 40% HF aqueous solution (60 mL) at room temperature and stirring for 3 days, the precipitate was collected by centrifugation, washed with water and ethanol, and then dispersed in 50 mL of tetrapropylammonium hydroxide. The dispersion was stirred at room temperature for another 3 days. Subsequently, the Ti_3C_2 was collected by centrifugation and washed three times with ethanol and water to remove any remaining tetrapropylammonium hydroxide.

Synthesis of Ti_3C_2@MSNs Composite Nanosheets

A solution of cetyltrimethylammonium chloride (CTAC) (10g, 10wt%) and triethanolamine (TEA) (0.2g, 10wt%) was pre-mixed and stirred in a room temperature water bath for 20 minutes. Subsequently, an aqueous solution of Ti_3C_2

 https://doi.org/10.2147/IJN.S487405

(10mg) was added dropwise (1 mg/mL, 10 mL), and the mixture was stirred for 1.5 hours under the same conditions followed by 20 minutes of sonication. Then, tetraethyl orthosilicate (TEOS) (150 μL) was added to the reaction system, and the mixture was stirred at 80°C for an additional hour to form the Ti_3C_2@MSNs structure. The product was collected by centrifugation, and washed three times with ethanol.

The structure-directing agent CTAC was extracted in a mixture of methanol and NaCl (8%) (50 mL, methanol: NaCl = 50 mL: 0.4g) at room temperature for 12 hours to remove it. Subsequently, the product was washed three times with ethanol, dispersed in ethanol, washed twice with deionized water, and finally dispersed in deionized water.

Synthesis of BZ-Ti_3C_2@MSNs Composite Nanosheets

The collected Ti_3C_2@MSNs was dispersed in an ethanol solution of mPEG-Silane ($W_{Ti3C2@MSNs}$: $W_{mPEG\text{-}Silane}$ = 1:3) and stirred for 12 hours. Ethanol and deionized water were used for multiple washings to remove the mPEG-Silane. The resulting product was redissolved in deionized water, Bevacizumab (BZ) was added at different feeding ratios, and the mixture was stirred overnight. Subsequent centrifugation yielded BZ-Ti_3C_2@MSNs. For thermal-responsive drug releasing analysis, the solution was irradiated with 808 nm laser for 5 min at varied power densities, followed by UV-vis analysis.

Characterization

Transmission electron microscopy (TEM) photographs were recorded on a field-emission FEI Talos F200S G2 microscope (FEI, USA). X-ray photoelectron spectroscopy (XPS) spectrum of Ti_3C_2@MSNs was conducted on a K-Alpha Nexsa (Thermal Scientific, USA). The X-ray diffraction (XRD) pattern of Ti_3C_2 was determined by D8 ADVANCE X-ray powder diffraction (Bruker, Germany) using Cu Kα radiation (λ=1.5406 Å) at 40 kV and 40 mA. Dynamic light scattering (DLS) was conducted on Brookhaven Instruments (NanoBrook Omni) for zeta potential and hydrodynamic particle size determination. UV−vis spectra was observed using a UV-3600 Plus Shimadzu spectroscope. The Ti_3C_2@MSNs concentration was determined by inductively coupled plasma Optical emission spectroscopy (ICP-OES Avio 200, PerkinElmer). Atomic force microscope (AFM) images were obtained from Bruker Dimension Icon.

In vitro Photothermal Performance

400 μL Ti_3C_2@MSNs solutions were added to 48-well plates and irradiated at power densities of 1.0 W/cm^2, 1.25 W/cm^2, and 1.5 W/cm^2 to evaluate the in vitro photothermal properties. NIR laser was generated by an 808 nm laser (MDL-XF-808, CNI, China). The site temperature and the corresponding thermal photographs were recorded by an infrared camera (618C, FOTRIC, China). The photothermal performance of Ti_3C_2@MSNs was measured at a power density of 1.25 W/cm^2.

Calculation of the Extinction Coefficient

The extinction coefficient at 808 nm was measured based on the Lambert-Beer law (A/L = αC, where α is the extinction coefficient). A linear relationship between A/L and concentration (C) was observed at various concentrations (5, 10, 25, 50, and 100 μg/mL) under the wavelength λ = 808 nm. Subsequently, the extinction coefficient was determined.

Calculation of Photothermal Conversion Efficiency

Based on previous reports,[35,36] the total energy balance in the system can be calculated as:

$$\sum_i m_i C_{p,i} \frac{dT}{dt} = Q_{Ti_3C_2@MSNs} + Q_{Dis} - Q_{surr} \quad (1)$$

m_i, and $C_{p,i}$ represents the mass and specific heat capacity of the solvent (water) respectively, T represents the temperature of the solution, $Q_{Ti3C2@MSNs}$ signifies the input energy of the Ti_3C_2@MSNs nanocomposite material, Q_{Dis} represents the heat lost by the system due to light absorption, and Q_{surr} represents the energy exiting the system through the air. When the laser power is constant, $Q_{Ti3C2@MSNs} + Q_{Dis}$ can be computed.

Under 808 nm laser irradiation, $Q_{Ti3C2@MSNs}$ can be expressed as:

$$Q_{Ti_3C_2@MSNs} = P\left(1 - 10^{-A_{808}}\right)\eta \quad (2)$$

P represents incident energy of NIR laser (mW); η represents the photothermal conversion efficiency of Ti_3C_2@MSNs nanocomposite material; A_{808} represents the absorbance of the nanosheets at 808 nm.
Q_{surr} can be expressed as:

$$Q_{surr} = hS(T - T_{surr}) \quad (3)$$

h represents heat-transfer coefficient, *S* represents the surface area of the container, *T* represents the temperature of the system surface, and T_{surr} represents the surrounding temperature.

Since the heat output (T_{surr}) was increased along with the rise in temperature of the system, a maximum amount would be reached when the heat output was equal to heat input:

$$Q_{Ti_3C_2@MSNs} + Q_{Dis} = Q_{surr-max} = hS(T_{max} - T_{surr}) \quad (4)$$

$Q_{surr\text{-}max}$ represents the heat transferred outward through the air when the system reaches equilibrium temperature, T_{max} represents the equilibrium temperature.

By combining equations (1) to (4), the formula for calculating the photothermal conversion efficiency (η) can be derived as:

$$\eta = \frac{hS(T_{max} - T_{surr}) - Q_{Dis}}{P\left(1 - 10^{-A_{808}}\right)} \quad (5)$$

The calculation formula for the driving temperature θ of the Ti_3C_2@MSNs aqueous solution was given by:

$$\theta = \frac{T - T_{surr}}{T_{max} - T_{surr}} \quad (6)$$

The time constant of sample system, τ_s was calculated as:

$$\tau s = \frac{\sum_i m_i C_{p,i}}{hS} \quad (7)$$

Based on the above formula, τ_s can be recalculated as:

$$\tau_s = -\frac{t}{\ln(\theta)} \quad (8)$$

The time constant of sample system can be determined through linear time data from the system's cooling phase, in conjunction with the negative logarithm of the driving temperature θ. Therefore, the constant of heat transfer from the system was determined to be τ_s =136.3 s of 808 nm. In addition, the *m* was 0.4 g and the $C_{p,i}$ was 4.2 J/g. Substituting *h*S into equation (5), the photothermal-conversion efficiency (η) of Ti_3C_2@MSNs at 808 nm could be calculated to be 27.7%.

Hemolytic Activity Test

Erythrocytes were diluted by PBS to the final concentration of 5% (v/v). 500 μL sample and 500 μL erythrocytes were added to the 1.5 mL centrifugal tube, and then incubated in an incubator 1 h at 37°C with shaking speed of 100 rpm. The experiment was divided into 5 groups, including Ti_3C_2, Ti_3C_2@MSNs, BZ, and BZ-Ti_3C_2@MSNs. PBS buffer was used as a negative control, and 0.1% Triton x-100 was used as a positive control. The absorbance of the solution was read by a microplate reader (Infinite E Plex, Tecan, Switzerland) at 540 nm。 The hemolysis percentage was calculated from the relation: Hemolysis (%) = [(Ae– Ab)/(Ap–Ab)] × 100%, where Ae was the absorbance value for the experiment group. Ap was the absorbance value for the Triton x-100 positive control and Ab was the absorbance value for PBS negative control.

In vitro Cytotoxicity Assay

4T1 cells, purchased from SUNNCELL Biotechnology (Wuhan, China), were cultured in Roswell Park Memorial Institute 1640 (RPMI 1640, Gibco) containing 10% fetal bovine serum (FBS, Biological Industries) and 1% penicillin-streptomycin (Gibco) at 37 °C in CO_2 incubator. To determine the cell viability of 4T1 cells after various

 https://doi.org/10.2147/IJN.S487405

treatments, the cells were seeded in a 96-well plate (5×10^3 cells/well) and incubated for 24 h. A serial of diluents containing Ti_3C_2 and Ti_3C_2@MSNs at different concentrations was co-incubated with 4T1 cells pre-seeded in 96-well plates for 24 and 48 h. The medium was replaced with a new 100 μL RPMI 1640 medium, and then 10 μL CCK-8 (Beyotime, China) was added to each hole, and continued to incubate 1 h at 37°C in CO_2 incubator. Afterwards, the microplate reader (Infinite E Plex, Tecan, Switzerland) was used to determine the absorbance of the solution at 450 nm.

In vitro Photothermal Ablation of 4T1 Cells and Fluorescence Imaging Assay

To determine the cell viability of 4T1 cells after various treatments, the cells were seeded in a 96-well plate (5×10^3 cells/well) and incubated for 24 h. A serial of diluents containing Ti_3C_2, Ti_3C_2@MSNs, and BZ-Ti_3C_2@MSNs at different concentrations was co-incubated with 4T1 cells pre-seeded in 96-well plates for 24 h. After that, the solutions were irradiated with 808 nm laser at different power densities (1.0, 1.25, or 1.5 W/cm^2) for 5 min, and then CCK-8 assay was used to evaluate the cell viability after treatments. For fluorescence imaging, 4T1 cells were seeded in 48-well plates (3×10^4 cells/well) and divided into six treatment groups (Control, Ti_3C_2, Ti_3C_2@MSNs, BZ, BZ-Ti_3C_2@MSNs, and BZ-Ti_3C_2@MSNs + NIR). After different treatments, cells were stained with Calcein/PI for 30 min. Finally, the fluorescence photographs were recorded on a fluorescence microscope (ECLIPSE Ts2R-FL, Nikon, Japan).

Intracellular Endocytosis by CLSM Observation

To obtain Ti_3C_2@MSNs-FITC, Ti_3C_2@MSNs was stirred with fluorescein isothiocyanate (FITC, 5mg, Sigma-Aldrich, Shanghai, China) at room temperature overnight. 4T1 cells were seeded in a confocal laser scanning microscopy (CLSM)-specific dishes and incubated for 24 h. The cells were then co-incubated with Ti_3C_2@MSNs-FITC for 2, 4, and 8 h. Subsequently, the cell nuclei were stained with DAPI and the cells were observed using CLSM. Similarly, to assess the endocytic uptake of BZ, 4T1 cells were initially seeded in CLSM-specific dishes and divided into four treatment groups: Control group, free BZ group, BZ-Ti_3C_2@MSNs group, and BZ-Ti_3C_2@MSNs + NIR group. Following this, the cells were stained with DAPI, and their visualization was carried out using confocal laser scanning microscopy (CLSM).

In vivo Blood Circulation and Biodistribution

All animal procedures were performed under the guidelines approved by the Ethic Committee of the Shandong Cancer Hospital and Institute (No. SDTHEC2024005039). To evaluate the in vivo blood circulation of Ti_3C_2@MSNs, female KM mice were intravenously injected with Ti_3C_2@MSNs in PBS (n = 4). Blood sample of 10 μL was collected at varied time (1min, 3 min, 15 min, 30 min, 1 h, 2 h, 4 h, 8 h, 12 h, and 24 h). The blood was collected into 1 mL of physiological saline containing heparin sodium (50 unit/mL). The concentration of Ti was then measured by ICP-OES. Subsequently, the in vivo blood terminal half-life of Ti_3C_2@MSNs was calculated using a double-component pharmacokinetic model. Nude mice pre-inoculated with 4T1 cells (tumor volume = 100 mm^3) were intravenously injected with Ti_3C_2@MSNs (dissolved in PBS, 100 μL). Subsequently, mice were euthanized at predetermined time points, and major organs and tumors were excised, weighed, and homogenized. The distribution of Ti_3C_2@MSNs in major organs and tumors was calculated as a percentage of the injected dose per gram of tissue.

In vivo Tumor Therapy Assay

Female Balb/c Nude mice (4 weeks old), obtained from Vital River (China), were used for studies. All mice were randomly divided into five groups (n = 5), including the Control group, Ti_3C_2@MSNs group, NIR group, BZ group, and BZ-Ti_3C_2@MSNs + NIR group. First, 4T1 cells (2×10^6 cells, suspended in PBS) were injected subcutaneously into mice. The tumor continued to grow to reach an average volume of approximately 100 mm^3. The time interval between intravenous injection and laser irradiation was set at 4 h. The tumor volume was calculated as: length × width × width/2. After treatment for 14 days, the tumor was harvested for pathological histology analysis. The tumor growth inhibition

value (TGI) was calculated from the relation: TGI (%) = (1–We/Wc) × 100%, where We was the tumor weight value for the experiment group. Wc was the tumor weight value for the control group.

Statistical Analysis

The values were expressed as mean ± standard deviation, and $P < 0.05$ was considered statistically significant (*$P < 0.05$, *$P < 0.01$, *$P < 0.001$).

Results and Discussion

Synthesis and Characterization of Ti_3C_2@MSNs

A Ti_3C_2 MXene-based Ti_3C_2@MSNs was prepared using a sol-gel method based on mesoporous silica coating. A double-layered Ti_3AlC_2 MAX phase ceramic, including initial hydrofluoric acid (HF) etching and subsequent tetrapropylammonium hydroxide (TPAOH) intercalation, was employed to synthesize ultra-thin two-dimensional Ti_3C_2 MXene nanosheets using a typical two-step delamination process. To delaminate the MAX phase ceramic, HF-etched Ti_3C_2 powder was dispersed in water with TPAOH intercalation. It was found that prolonged HF etching and subsequent TPAOH intercalation significantly reduced the planar dimensions of Ti_3C_2 nanosheets. After further insertion of TPAOH, transmission electron microscopy (TEM) images showed thin and transparent detached Ti_3C_2 nanosheets (Figure 1a), indicating a typical two-dimensional sheet-like structure with high dispersibility. The X-ray diffraction (XRD) pattern of the synthesized Ti_3C_2 nanosheets is shown in Figure 1b. The formation of the main characteristic peak ($2\theta \approx 6°$) of Ti_3C_2 nanosheets indicates the successful delamination of three-dimensional Ti_3AlC_2 ceramics into two-dimensional ultra-thin Ti_3C_2 nanosheets. The synthesized ultra-thin Ti_3C_2 nanosheets' surface contains abundant hydroxyl groups, and the negatively charged nanosheet surface further couples with positively charged CTAC (pore-forming agent) through electrostatic interactions. Subsequently introduced TEOS as a silica source, hydrolyzed self-assembled with surface-adsorbed CTAC, and grew mesoporous silica layer in situ on the Ti_3C_2 MXene surface under alkaline conditions. A uniformly coated mesoporous silica layer was observed on the surface of Ti_3C_2 nanosheets, as shown in TEM images (Figure 1c). Specifically, all Ti_3C_2 nanosheets in the synthetic system could be enveloped by mesoporous silica layer, and abundant mesopores were observed on the surface of Ti_3C_2@MSNs, directly proving the penetration of mesopores onto the surface and facilitating the loading and release of guest molecules. The uniform distribution of ultra-thin Ti_3C_2 nanosheets in Ti_3C_2@MSNs was further confirmed by corresponding elemental mapping (Figure 1d, S1 and S2), clearly showing the planar distribution of Ti components in the entire composite MXene nanosheets and the thickness of Ti_3C_2 and Ti_3C_2@MSNs nanosheets determined by atomic force microscopy (AFM) is less than 20 nm (Figure S3a–d). The chemical composition of Ti_3C_2@mMSNs was further determined by X-ray photoelectron spectroscopy. The characteristic peak at 103.5 eV indicates the Si-O bond, reflecting the presence of mesoporous silica layer on Ti_3C_2 nanosheets (Figure 1e and S4). The characteristic peaks at 532.28 eV and 530.38 eV point to O 1s, while the peaks at 455.2 and 463.8 correspond to Ti-C and Ti-O bonds, respectively (Figure 1f and g).

In vitro Photothermal Properties of Ti_3C_2@MSNs

The hydrodynamic diameter and zeta potential of Ti_3C_2 and Ti_3C_2@MSNs were determined. The average particle size of Ti_3C_2 and Ti_3C_2@MSNs (Figure 2a) was around 203 nm and 237 nm as measured by dynamic light scattering (DLS), with the increased size attributed to the surface coating of MSN. Following a seven-day incubation period in both PBS and RPMI 1640 media, the particle size of Ti_3C_2@MSNs remained consistent, with no significant differences observed (Figure S5). A series of changes in zeta potential at each step revealed the successful binding of MSNs with Ti_3C_2 nanosheets (Figure 2b). The results indicated that the zeta potential of Ti_3C_2 decreased from −21.8 mV to −28.8 mV due to the modification with MSNs. Initially, Ti_3C_2@mMSNs composite nanosheets were expected to have high photothermal conversion capability, given the presence of 2D Ti_3C_2 MXene in the core. At different concentrations (5, 10, 25, 50, and 100 μg/mL), the extinction coefficient of Ti_3C_2@mMSNs at 808 nm was found to be 5.79 Lg^{-1} cm^{-1} (Figure 2c and d), significantly higher than most explored graphene oxide nanosheets (3.6 Lg^{-1} cm^{-1}), indicating that the mesoporous silica coating could still maintain the high photothermal conversion performance of Ti_3C_2 MXene. The

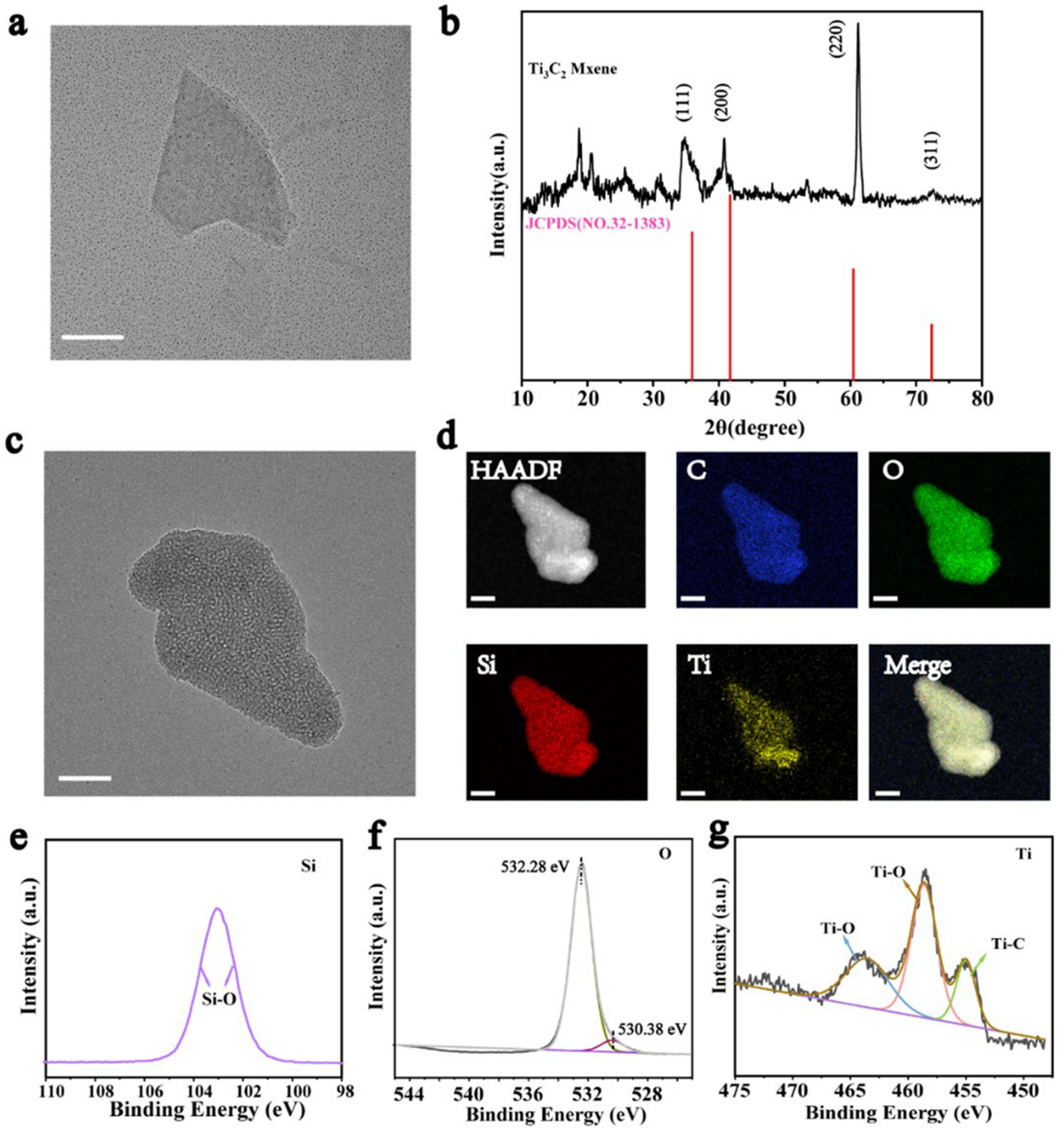

Figure 1 Synthesis and characterization of Ti_3C_2@MSNs composite nanosheets. (**a**) TEM image of Ti_3C_2. Scale bar:100 nm (**b**) XRD pattern of Ti_3C_2. (**c**) TEM image of Ti_3C_2@MSNs. (**d**) The corresponding elemental mappings of C, O, Si and Ti. Scale bar: 50 nm. (**e**) X-ray photoelectron spectroscopy (XPS) of Ti_3C_2@MSNs. (**f**) High-resolution O 1s and (**g**) Ti 2p spectra of Ti_3C_2@MSNs.

photothermal conversion efficiency (η) of Ti_3C_2@mMSNs nanosheets was calculated to be 27.7% (Figure 2e and f), comparable to traditional Au nanosheets (21%) and $Cu_{2-x}Se$ NCs (22%). The photothermal efficiency is still sufficiently high for tumor ablation. To evaluate the photothermal conversion performance of Ti_3C_2@MSNs, photothermal performance tests were conducted at different power densities (0.5, 1.0, 1.25, and 1.5 W cm^{-2}) with a fixed concentration of 200 μg mL^{-1} (Figure 2g). Different concentrations were irradiated under 808 nm near-infrared laser (1.5 W cm^{-2}) for 5 minutes (Figure 2h). The results showed that the temperature of Ti_3C_2@MSNs reached 60°C after 5 minutes of

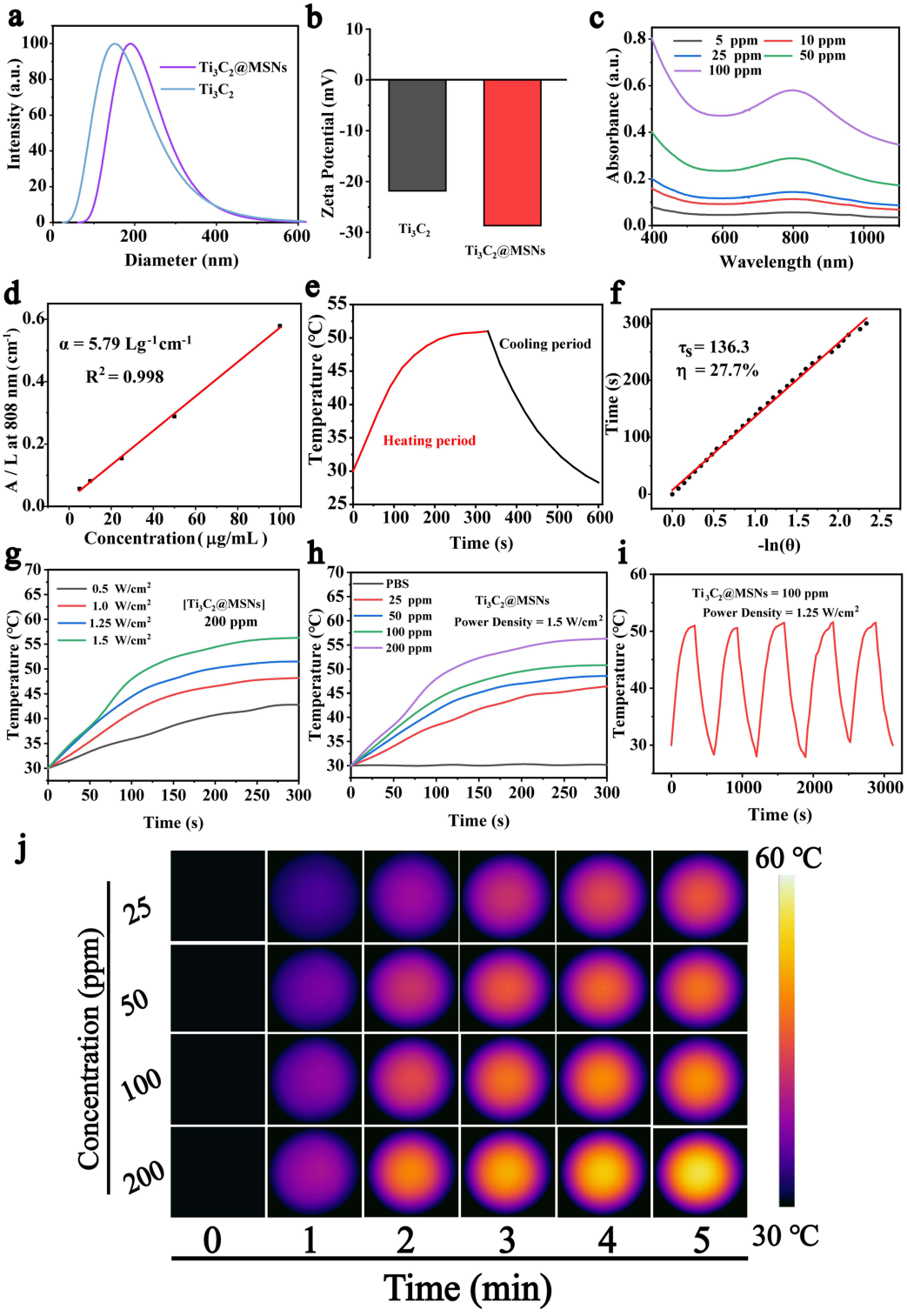

Figure 2 Characterization and Photothermal properties of Ti_3C_2@MSNs. (**a**) Particle-size distribution of Ti_3C_2 and Ti_3C_2@MSNs. (**b**) Zeta potential of Ti_3C_2 and Ti_3C_2@MSNs. (**c**) UV-vis spectra of Ti_3C_2@MSNs dispersed in aqueous solution at varied concentrations (5, 10, 25, 50, and 100 μg/mL). d) Normalized absorbance intensity at λ = 808 nm divided by the characteristic length of the cell (A/L) at varied concentrations (5, 10, 25, 50, and 100 μg/mL). (**e**) Photothermal effect of aqueous dispersion of Ti_3C_2@MSNs under irradiation by NIR laser (808 nm, 1.25 W cm^{-2}). (**f**) Time constant for heat transfer from the system was determined to be 136.3 s by applying the linear time data from the cooling period versus negative natural logarithm of driving force temperature, which was originated from the cooling stage. (**g**) Photothermal-heating curves of Ti_3C_2@MSNs under varied power densities (0.5, 1.0, 1.25, and 1.5 W cm^{-2}). (**h**) Photothermal heating curves of Ti_3C_2@MSNs at different concentrations upon exposure to 808 nm laser irradiation (1.5 W cm^{-2}). (**i**) Temperature profiles of Ti_3C_2@MSNs with laser irradiation (P = 1.25 W cm^{-2}) for five laser on/off cycles. (**j**) Infrared thermographic maps of Ti_3C_2@MSNs at varied concentrations (25, 50, 100, and 200 μg/mL) under NIR irradiation (1.25 W cm^{-2}).

https://doi.org/10.2147/IJN.S487405

irradiation. In contrast, the temperature of the PBS solution remained almost unchanged, indicating that the presence of Ti_3C_2@mMSNs composite nanosheets could effectively and rapidly convert near-infrared light into heat, possibly due to the enhancement of material hydrophilicity and dispersibility by the mesoporous silica coating. To evaluate photothermal stability, five heating/cooling cycles were tested (Figure 2i), with no significant temperature decrease observed, indicating that Ti_3C_2@mMSNs have high photothermal stability and can serve as durable photothermal agents for photothermal therapy. The photothermal conversion performance of Ti_3C_2@MSNs at different concentrations was evaluated under 808 nm laser irradiation (1.25 W cm^{-2}), and thermal images were recorded using an infrared thermal imager, showing similar photothermal conversion capabilities (Figure 2j).

In vitro Drug-Loading Capacity and Chemophotothermal Synergistic Therapy Against TNBC Cells of BZ-Loaded Ti_3C_2@MSNs

Inspired by the well-defined mesoporous structure of Ti_3C_2@MSNs, we further investigated its drug loading properties and drug release behavior. The typical chemotherapeutic drug, Bevacizumab (BZ), was selected to evaluate the drug delivery performance of Ti_3C_2@mMSNs. The drug loading amount of Ti_3C_2@MSNs after BZ loading was determined by UV-visible spectroscopy of the supernatant. With an increasing feed ratio of BZ- Ti_3C_2@MSNs, the loading capacity of BZ increased, reaching a maximum loading amount of 43.5% (Figure 3a). Importantly, localized hyperthermia-induced BZ release under near-infrared laser irradiation could also be observed at different time points, achieving a release of 35.0% (1.25 W cm^{-2}) at pH 7.4, under the open/close control of near-infrared irradiation (Figure 3b). In particular, an increase in power density could trigger significantly more drug release by achieving higher local temperatures. The significant enhancement of cumulative drug release may be attributed to the thermally induced dissociation of the strong binding between BZ and Ti_3C_2@mMSNs. Photothermal therapy has emerged as a promising

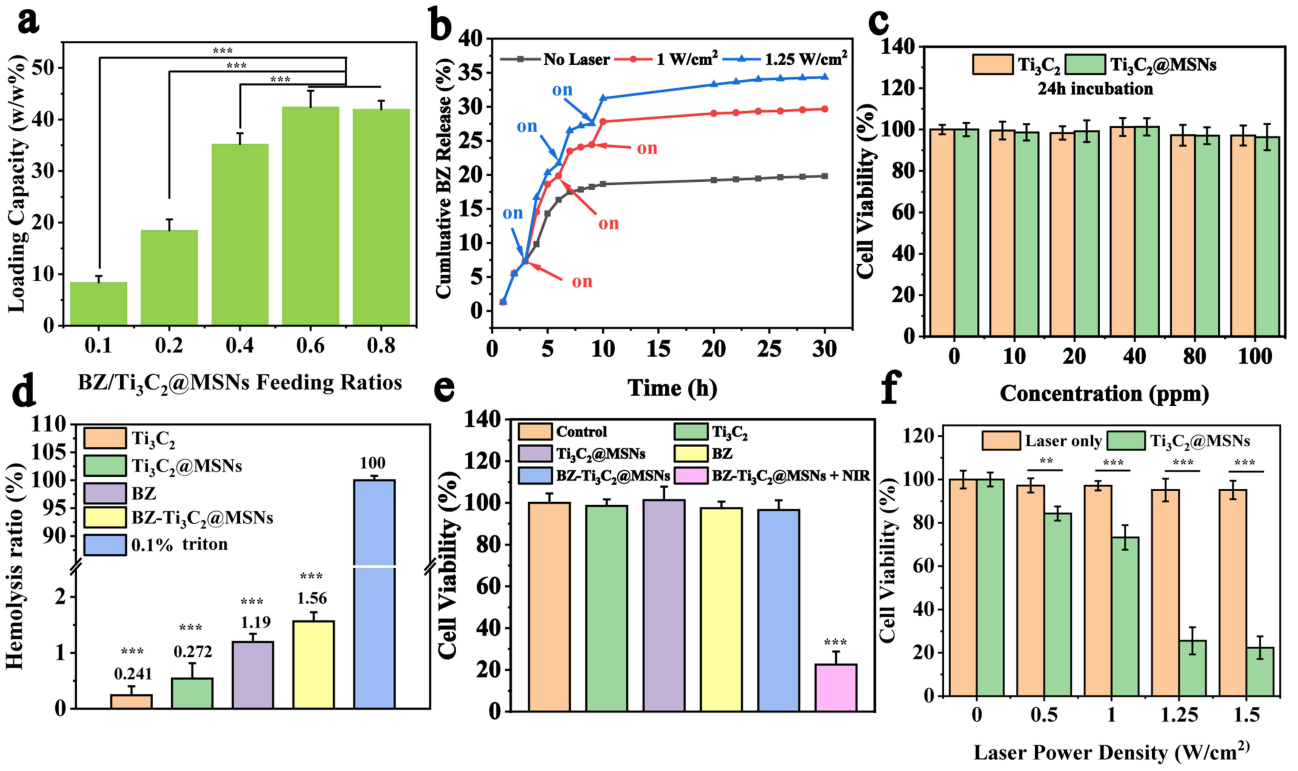

Figure 3 Drug-loading capacity and stimuli-responsive release of BZ-loaded Ti_3C_2@MSNs. In vitro chemophotothermal synergistic therapy against 4T1 cells. (**a**) BZ-loading capacities on Ti_3C_2@MSNs (w/w%) with elevated BZ-Ti_3C_2@MSNs (n = 3). (**b**) Cumulative BZ release from BZ-Ti_3C_2@MSNs in PBS (pH = 7.4) as triggered by 808 nm NIR lasers at elevated power density (n = 3). (**c**) Cytotoxicity of Ti_3C_2 and Ti_3C_2@MSNs after the incubation with 4T1 cell lines for 24 h (n = 6). (**d**) Hemolytic percentage of Ti_3C_2, Ti_3C_2@MSNs, BZ, and BZ-Ti_3C_2@MSNs (n = 3). (**e**) Relative cell viability of 4T1 cells incubated in the presence of 100 μg/mL of Ti_3C_2, Ti_3C_2@MSNs, BZ, and BZ-Ti_3C_2@MSNs with or without laser irradiation (n = 6). (**f**) Relative cell viability of 4T1 cells treated with different NIR power densities in the presence of Ti_3C_2@MSNs (n = 6). Statistical significances were calculated via Student's *t* test. **p < 0.01, and ***p < 0.001.

treatment modality for solid tumors, with liposome-based thermally triggered drug release patterns being extensively investigated. However, Phase III trials using liposomes for the treatment of TNBC failed due to their instability in serum. The NIR-triggered release characteristics and excellent stability of Ti_3C_2@MSNs make it an ideal drug delivery nanosystem, providing a basis for further in vitro and in vivo experiments on photodynamic therapy. Given the ideal in vitro photothermal conversion properties and the stimulant-responsive release of BZ, we investigated the targeted synergistic effect of photothermal hyperthermia and chemotherapy with BZ-loaded Ti_3C_2@mMSNs in TNBC cell lines. First, the cytotoxicity profile of Ti_3C_2@MSNs was evaluated (Figure 3c, S6). Although there was a slight increase in toxicity after mesoporous silica coating, no significant cytotoxicity was observed at a high concentration of 100 ppm after co-incubation for 24 h and 48 h, indicating the high biocompatibility of Ti_3C_2@MSNs. Excellent biocompatibility is an essential factor for the application of biomaterials. In vitro hemolysis test was performed to estimate the hemocompatibility of Ti_3C_2@MSNs. The quantitative data are presented in Figure 3d. All groups exhibited a very low hemolysis ratio (< 5%), indicating the good hemocompatibility. The potential toxicity of BZ to normal tissues limits its further application. Considering the insufficient inhibitory effect of chemotherapy on tumor cells, the efficacy of photothermal therapy is relatively high, further evaluating the synergistic effect of combined chemotherapy and PTT. As expected, even at a very low concentration of 100 μg mL^{-1}, the inhibitory efficiency of BZ was significantly enhanced by delivering BZ-loaded Ti_3C_2@mMSNs and performing photothermal ablation (Figure 3e). The IC50 of Ti_3C_2@MSNs combined with PTT for 4T1 cells was determined to be 45.3 μg/mL (Figure S7). Then, the photothermal ablation efficiency of Ti_3C_2@MSNs under 808 nm laser irradiation at different power densities was evaluated (Figure 3f). It is worth noting that Ti_3C_2@MSNs showed significant advantages in suppressing TNBC cell growth.

In vitro Synergistic PTT-Chemotherapy

In order to understand the mechanism of enhanced TNBC inhibition by Ti_3C_2@mMSNs in vitro, the cellular uptake of Ti_3C_2@MSNs was investigated. The process of cellular uptake was time-dependent, with an increase in green fluorescence intensity observed at longer incubation times (2, 4, and 8 hours) (Figure 4a). The targeting capability of Ti_3C_2@MSNs was evaluated utilizing flow cytometry analysis. Furthermore, we quantified the relative fluorescence intensity, the findings of which are illustrated in Figure S8a and b. Notably, the relative fluorescence intensity exhibited a substantial increase at the 2, 4, and 8-hour marks. Furthermore, confocal microscopy imaging further confirmed cell apoptosis after chemophotothermal therapy (Figure 4b). TNBC 4T1 cells were co-incubated with the nanomaterial for 24 h, followed by 10 minutes of 808 nm laser irradiation, and live and dead cells were stained with calcein-AM (green) and propidium iodide (PI) (red), respectively. Under 808 nm laser irradiation, most apoptotic cells treated with BZ-Ti_3C_2@MSNs showed strong red fluorescence, indicating a significant enhancement of cell apoptosis after chemotherapy. Importantly, the advantage of Ti_3C_2@MSNs in cell apoptosis can be attributed to its TNBC-specific targeting effect, as confirmed by co-incubation for 24 h. To investigate the mechanism of cell death, flow cytometry analysis (Figure 4c) revealed that cell death induced by the synergistic treatment with BZ-Ti_3C_2@MSNs was primarily due to direct death and late-stage apoptosis.

In vivo Pharmacokinetic and Biodistribution Analysis, and Synergistic Chemotherapy/PTT Against TNBC-Tumor-Bearing Mice

Biodistribution experiments in vivo indicate that Ti_3C_2@MSNs can effectively accumulate in tumor tissues 4 hours after intravenous injection, with a targeting rate of 17.21% (Figure 5a). Ti_3C_2@MSNs mainly existed in the liver and spleen. There was the highest accumulation of silicon in tumors 4 h postintravenous injection. Then silicon content in tumors decreased slowly and even after 48 h Ti_3C_2@MSNs still contained in tumors. The blood circulation half-life of Ti_3C_2@MSNs is calculated to be 0.98 hours (Figure 5b). The effective active targeting ability of Ti_3C_2@MSNs may ensure its further high therapeutic efficacy in vivo. During the treatment period, the weight fluctuations of all mice were negligible (Figure 5c), indicating that the injection dose had minimal adverse effects on the overall health of the mice. In the control group, the tumor volume of the group treated with only near-infrared laser and the group treated with only BZ increased rapidly over 14 days, whereas the therapeutic effect of free BZ- Ti_3C_2@MSNs at the same dose was better

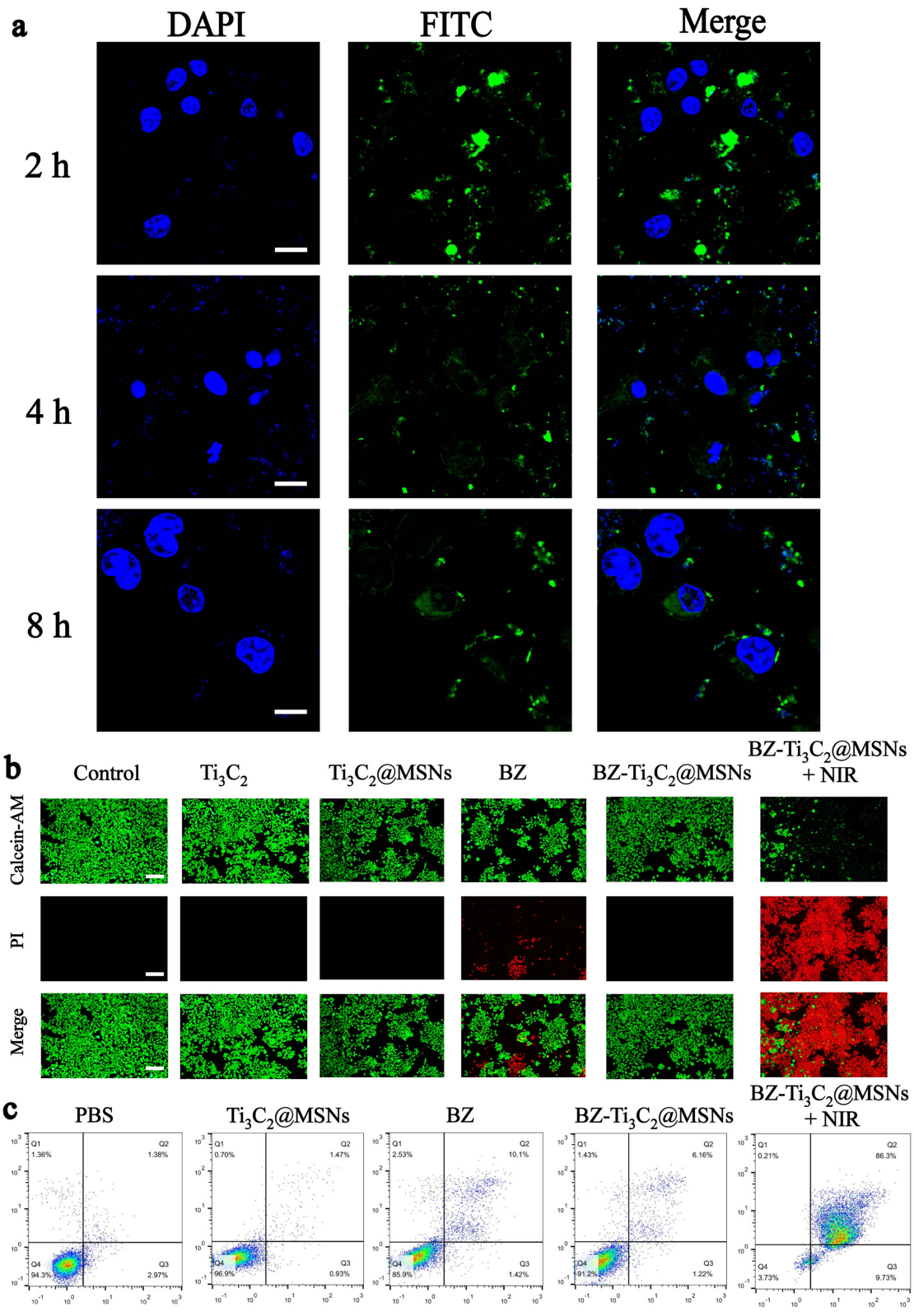

Figure 4 In vitro intracellular drug delivery and synergistic chemotherapy and PTT. (**a**) CLSM images of cellular uptake of FITC-labeled Ti_3C_2@MSNs (green) after 4T1 TNBC cells (blue) incubation at different time points. Scale bars: 25 μm. (**b**) CLSM images of 4T1 cells after different treatments, including control group, Ti_3C_2 group, Ti_3C_2@MSNs group, BZ only group, BZ-Ti_3C_2@MSNs group, and BZ-Ti_3C_2@MSNs + NIR group. The red fluorescence represents dead cells and green fluorescence represents live cells. (**c**) Flow cytometry study of 4T1 cells treated separately with PBS, Ti_3C_2@MSNs, BZ, BZ- Ti_3C_2@MSNs, and BZ-Ti_3C_2@MSNs + NIR.

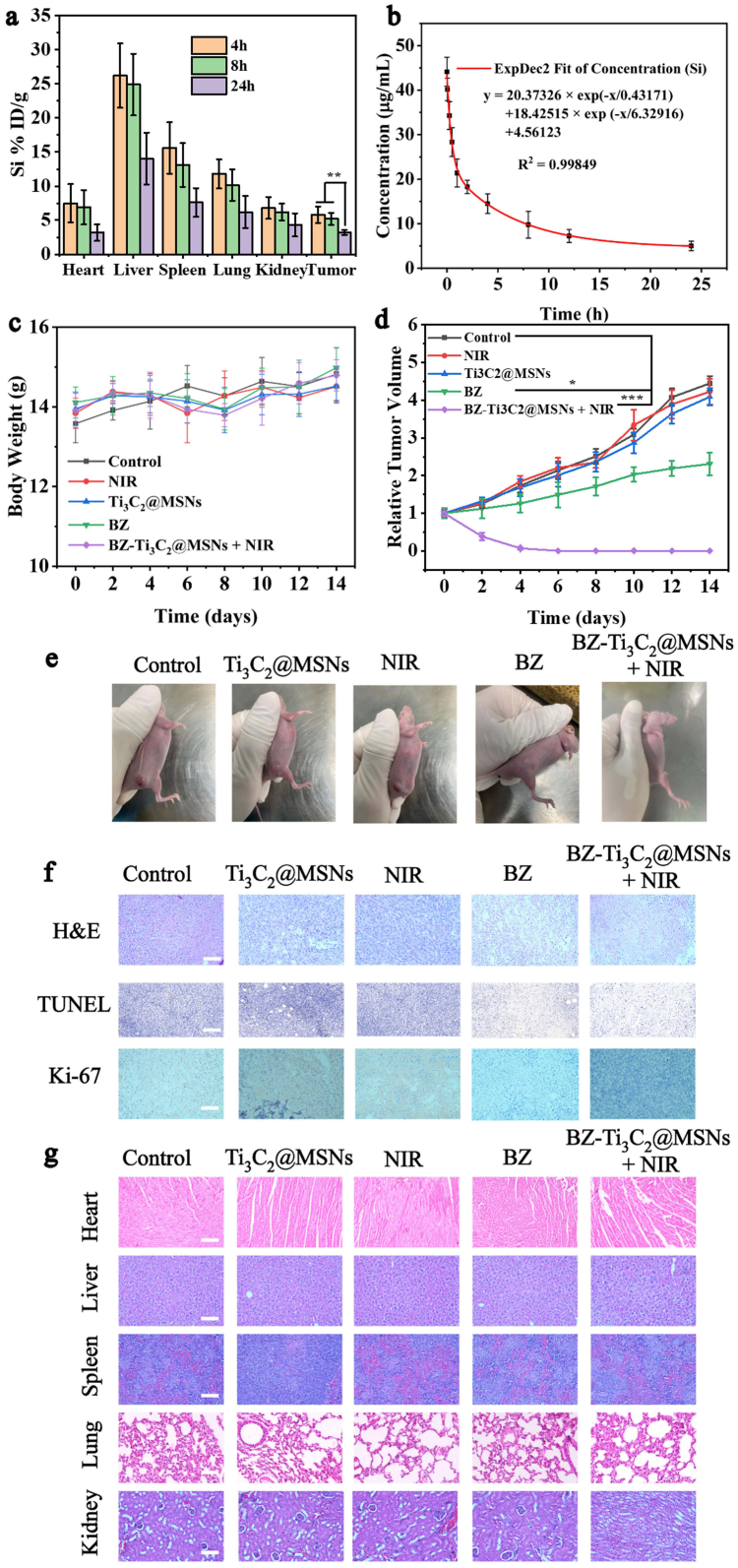

Figure 5 In vivo pharmacokinetic and biodistribution analysis, and synergistic PTT against tumor-bearing mice. (**a**) The biodistribution of Si in the major organs and tumor of tumor-bearing mice after the intravenous injection of Ti_3C_2@MSNs for 4, 8 h, and 24 h. (**b**) Blood circulation lifetime of Ti_3C_2@MSNs after intravenous injection into mice (n = 3). The half-time ($T_{1/2}$) was calculated to be approximately 1.08 h. (**c**) Time-dependent body-weight curves of nude mice after different treatments. d) Relative tumor volume of mice in each group after treatments for 14 days. (**e**) Photographs of 4T1 tumor-bearing mice and its tumor regions in 14 days after different treatments. (**f**) Histological analysis, including H&E, TUNEL, and Ki-67 staining, of tumor sections collected from different groups. Scale bar: 100 μm. (**g**) H&E-stained tissue sections of major organs (heart, liver, spleen, lung, and kidney) from mice with different treatments. Scale bar: 100 μm. Statistical significances were calculated via Student's *t* test. *p < 0.05, **p < 0.01, and ***p < 0.001.

https://doi.org/10.2147/IJN.S487405

(Figure 5d, e and S9), validating the benefits of the BZ-Ti_3C_2@MSNs drug delivery system. In addition, the synergistic photothermal chemotherapy group (BZ-Ti_3C_2@MSNs+NIR) exhibited significant the tumor inhibition rate (Figure S10). These targeted composite drug delivery nanosystems have the advantages of efficient drug loading, controllable and sustained drug release in the TNBC microenvironment, reducing the toxicity of chemotherapy to the body, and increasing the tumor inhibition rate. To further understand the synergistic therapeutic mechanisms after different treatments, tumor sections from each group of mice were collected 24 h after different treatments for hematoxylin and eosin (H&E) staining, TDT-mediated dUTP nick-end labeling (TUNEL), and Ki-67 antibody staining. H&E and TUNEL staining (Figure 5f) showed that compared to other groups, the synergistic photothermal chemotherapy group (BZ-Ti_3C_2@MSNs +NIR) exhibited significant apoptosis and necrosis in TNBC cells. The apoptosis rate of TNBC cells in the BZ-Ti_3C_2@MSNs+NIR group was significantly higher than that of mice injected with free BZ, further indicating that the nanosheets enhanced the inhibitory effect on TNBC. Through Ki-67 antibody staining to detect in vivo proliferative activity, the BZ- Ti_3C_2@MSNs+NIR group showed strong inhibitory effects on cell proliferation (Figure 5f), while other groups had no significant inhibitory effects on cancer cell proliferation. Based on the results of H&E and TUNEL staining, Ti_3C_2@MSNs+NIR had a greater inhibitory effect on Ki-67 than free BZ, indicating that Ti_3C_2@MSNs had a good inhibitory effect on chemotherapy through the drug delivery system. After 28 days, H&E staining images of major organs in each group showed no significant toxic side effects in mice during chemo-PTT (Figure 5g). Simultaneously, the examination of peripheral blood samples and subsequent blood biochemistry assays revealed no significant alterations in primary biochemical indicators, such as total protein (TP), mean corpuscular volume (MCV), albumin (ALB), alanine aminotransferase (ALT), aspartate aminotransferase (AST), alkaline phosphatase (ALP) and white blood cell (WBC), when compared to the control group that did not receive BZ-Ti_3C_2@MSNs (Figure S11).

Conclusions

In conclusion, we designed a surface nanopore engineering strategy to successfully construct a Ti_3C_2-based nanocomposite drug delivery system (BZ-Ti_3C_2@MSNs), which can effectively synergize tumor therapy. Compared with traditional two-dimensional MXene modification strategies, this system (BZ-Ti_3C_2@MSNs) has characteristics such as high photothermal conversion efficiency, drug loading capacity of up to 43.5%, near-infrared laser-triggered on-demand drug release, and enhanced biocompatibility. Systematic in vitro and in vivo experiments demonstrated that BZ-Ti_3C_2@MSNs exhibited a synergistic therapeutic effect on tumors through PTT (contributed by Ti_3C_2 MXene) and chemotherapy (contributed by mesopores), and by combining with the vascular factor inhibitor bevacizumab, achieving the goal of completely eradicating tumors and effectively inhibiting tumor recurrence and metastasis. The system's in vivo biocompatibility and excretion tests indicated that it has high tissue compatibility, low physiological toxicity, and is easily excreted. This work not only demonstrates the great potential of BZ-Ti_3C_2@MSNs as a multifunctional reagent for tumor therapy but also promotes the exploration of new modification strategies for Ti_3C_2 nanosheets.

Acknowledgments

This work was financially supported by Natural Science Foundation of Shandong Province (Grant No. ZR2021QH286).

Disclosure

The authors report no conflicts of interest in this work.

References

1. Schmid P, Cortes J, Dent R, et al. Event-free survival with pembrolizumab in early triple-negative breast cancer. *N Engl J Med*. 2022a;386(6):556–567. doi:10.1056/NEJMoa2112651
2. Schmid P, Cortes J, Dent R, et al. Pembrolizumab plus chemotherapy in advanced triple-negative breast cancer. *N Engl J Med*. 2022b;387(3):217–226. doi:10.1056/NEJMoa2202809
3. Li Y, Zhang H, Merkher Y, et al. Recent advances in therapeutic strategies for triple-negative breast cancer. *J Hematol Oncol*. 2022;15(1):121. doi:10.1186/s13045-022-01341-0
4. Guillen KP, Fujita M, Butterfield AJ, et al. A human breast cancer-derived xenograft and organoid platform for drug discovery and precision oncology. *Nat Cancer*. 2022;3(2):232–250. doi:10.1038/s43018-022-00337-6

5. Fang RH, Gao W, Zhang L. Targeting drugs to tumours using cell membrane-coated nanoparticles. *Nat Rev Clin Oncol*. 2023;20(1):33–48. doi:10.1038/s41571-022-00699-x
6. Zhao Z, Fang L, Xiao P, et al. Walking dead tumor cells for targeted drug delivery against lung metastasis of triple-negative breast cancer. *Adv Mater*. 2022;34(33):e2205462. doi:10.1002/adma.202205462
7. He P, Lei Q, Yang B, et al. Dual-stage irradiation of size-switchable albumin nanocluster for cascaded tumor enhanced penetration and photothermal therapy. *ACS Nano*. 2022;16(9):13919–13932. doi:10.1021/acsnano.2c02965
8. Chen Q, Zhang M, Huang H, et al. Single atom-doped nanosonosensitizers for mutually optimized sono/chemo-nanodynamic therapy of triple negative breast cancer. *Adv Sci*. 2023;10(6):e2206244. doi:10.1002/advs.202206244
9. Lu J, Song L, Feng S, et al. Nanozyme-mediated biocatalysis as a mitochondrial oxidative stress amplifier for tumor nanocatalytic immunotherapy. *Chem Eng J*. 2024;481:148270. doi:10.1016/j.cej.2023.148270
10. Feng S, Lu J, Wang K, et al. Advances in smart mesoporous carbon nanoplatforms for photothermal–enhanced synergistic cancer therapy. *Chem Eng J*. 2022;435:134886. doi:10.1016/j.cej.2022.134886
11. Song L, Zhao Q, Feng S, et al. Depolymerizable enzymatic cascade nanoreactor for self-enhancing targeting synergistic tumor therapy. *Adv Funct Mater*. 2024;2414121. doi:10.1002/adfm.202414121
12. Liu Y, Li Y, Koo S, et al. Versatile types of inorganic/organic NIR-IIa/IIb fluorophores: from strategic design toward molecular imaging and theranostics. *Chem Rev*. 2022;122(1):209–268. doi:10.1021/acs.chemrev.1c00553
13. Xu C, Pu K. Second near-infrared photothermal materials for combinational nanotheranostics. *Chem Soc Rev*. 2021;50(2):1111–1137. doi:10.1039/D0CS00664E
14. Jiang Y, Huang J, Xu C, Pu K. Activatable polymer nanoagonist for second near-infrared photothermal immunotherapy of cancer. *Nat Commun*. 2021;12(1):742. doi:10.1038/s41467-021-21047-0
15. Ouyang J, Xie A, Zhou J, et al. Minimally invasive nanomedicine: nanotechnology in photo-/ultrasound-/radiation-/magnetism-mediated therapy and imaging. *Chem Soc Rev*. 2022;51(12):4996–5041. doi:10.1039/D1CS01148K
16. Zhu Y, Wang W, Cheng J, et al. Stimuli-responsive manganese single-atom nanozyme for tumor therapy via integrated cascade reactions. *Angew Chem Int Ed Engl*. 2021;60(17):9480–9488. doi:10.1002/anie.202017152
17. VahidMohammadi A, Rosen J, Gogotsi Y. The world of two-dimensional carbides and nitrides (MXenes). *Science*. 2021;372(6547):eabf1581. doi:10.1126/science.abf1581
18. Ji X, Ge L, Liu C, et al. Capturing functional two-dimensional nanosheets from sandwich-structure vermiculite for cancer theranostics. *Nat Commun*. 2021;12(1):1124. doi:10.1038/s41467-021-21436-5
19. Li N, Wang Y, Li Y, Zhang C, Fang G. Recent advances in photothermal therapy at near-infrared-II based on 2D MXenes. *Small*. 2024;20(6):e2305645. doi:10.1002/smll.202305645
20. Wang D, Zhou C, Filatov AS, et al. Direct synthesis and chemical vapor deposition of 2D carbide and nitride MXenes. *Science*. 2023;379(6638):1242–1247. doi:10.1126/science.add9204
21. Seidi F, Arabi Shamsabadi A, Dadashi Firouzjaei M, et al. MXenes antibacterial properties and applications: a review and perspective. *Small*. 2023;19(14):e2206716. doi:10.1002/smll.202206716
22. Li H, Fan R, Zou B, Yan J, Shi Q, Guo G. Roles of MXenes in biomedical applications: recent developments and prospects. *J Nanobiotechnology*. 2023;21(1):73. doi:10.1186/s12951-023-01809-2
23. Solangi NH, Mazari SA, Mubarak NM, Karri RR, Rajamohan N, Vo DN. Recent trends in MXene-based material for biomedical applications. *Environ Res*. 2023;222:115337. doi:10.1016/j.envres.2023.115337
24. Deng X, Shao Z, Zhao Y. Solutions to the drawbacks of photothermal and photodynamic cancer therapy. *Adv Sci*. 2021;8(3):2002504. doi:10.1002/advs.202002504
25. Zhu Y, Wang Z, Zhao R, et al. Pt decorated Ti3C2Tx MXene with NIR-II light amplified nanozyme catalytic activity for efficient phototheranostics. *ACS Nano*. 2022;16(2):3105–3118. doi:10.1021/acsnano.1c10732
26. Huo J, Jia Q, Huang H, et al. Emerging photothermal-derived multimodal synergistic therapy in combating bacterial infections. *Chem Soc Rev*. 2021;50(15):8762–8789. doi:10.1039/D1CS00074H
27. Wang Y, Meng HM, Li Z. Near-infrared inorganic nanomaterial-based nanosystems for photothermal therapy. *Nanoscale*. 2021;13(19):8751–8772. doi:10.1039/D1NR00323B
28. Wang Q, Zhang X, Tang Y, et al. High-performance hybrid phototheranostics for NIR-IIb fluorescence imaging and NIR-II-excitable photothermal therapy. *Pharmaceutics*. 2023;15(8):2027. doi:10.3390/pharmaceutics15082027
29. Parihar A, Singhal A, Kumar N, Khan R, Khan MA, Srivastava AK. Next-generation intelligent MXene-based electrochemical aptasensors for point-of-care cancer diagnostics. *Nanomicro Lett*. 2022;14(1):100. doi:10.1007/s40820-022-00845-1
30. Xu Y, Wang Y, An J, et al. 2D-ultrathin MXene/DOXjade platform for iron chelation chemo-photothermal therapy. *Bioact Mater*. 2021;14:76–85. doi:10.1016/j.bioactmat.2021.12.011
31. Kelley RK, Rimassa L, Cheng AL, et al. Cabozantinib plus atezolizumab versus sorafenib for advanced hepatocellular carcinoma (COSMIC-312): a multicentre, open-label, randomised, Phase 3 trial. *Lancet Oncol*. 2022;23(8):995–1008. doi:10.1016/S1470-2045(22)00326-6
32. Zhu AX, Abbas AR, de Galarreta MR, et al. Molecular correlates of clinical response and resistance to atezolizumab in combination with bevacizumab in advanced hepatocellular carcinoma. *Nat Med*. 2022;28(8):1599–1611. doi:10.1038/s41591-022-01868-2
33. Shepherd JH, Ballman K, Polley MC, et al. CALGB 40603 (alliance): long-term outcomes and genomic correlates of response and survival after neoadjuvant chemotherapy with or without carboplatin and bevacizumab in triple-negative breast cancer. *J Clin Oncol*. 2022;40(12):1323–1334. doi:10.1200/JCO.21.01506
34. Quesada S, Jacot W. Maintenance endocrine therapy plus bevacizumab for advanced or metastatic breast cancer. *Lancet Oncol*. 2022;23(5):557–558. doi:10.1016/S1470-2045(22)00205-4
35. Zhao Q, Zhang Y, Yu T, et al. Tailored nanoplatforms with detachable 'meteorolite' for photothermal-enhanced programmed tumor therapy. *Carbon*. 2022;199:119–131. doi:10.1016/j.carbon.2022.07.073
36. Feng S, Mao Y, Wang X, Zhou M, Lu H, Zhao Q. Triple stimuli-responsive ZnO quantum dots-conjugated hollow mesoporous carbon nanoplatform for NIR-induced dual model antitumor therapy. *J Colloid Interface Sci*. 2020;559:51–64. doi:10.1016/j.jcis.2019.09.120